Draft version October 24, 2014
Preprint typeset using LaTeX style emulateapj v. 5/2/11

arXiv:1410.6159v1 [astro-ph.GA] 22 Oct 2014

HST EMISSION LINE GALAXIES AT $Z \sim 2$: THE MYSTERY OF NEON

Gregory R. Zeimann [1,2], Robin Ciardullo [1,2], Henry Gebhardt [1,2], Caryl Gronwall [1,2], Alex Hagen [1,2], Jonathan R. Trump [1,2,3], Joanna S. Bridge [1,2], Bin Luo [1,2], and Donald P. Schneider [1,2]

Draft version October 24, 2014

ABSTRACT

We use near-IR grism spectroscopy from the *Hubble Space Telescope* to examine the strength of [Ne III] λ3869 relative to Hβ, [O II] λ3727 and [O III] λ5007 in 236 low mass ($7.5 \lesssim \log(M_*/M_\odot) \lesssim 10.5$) star-forming galaxies in the redshift range $1.90 < z < 2.35$. By stacking the data by stellar mass, we show that the [Ne III]/[O II] ratios of the $z \sim 2$ universe are marginally higher than those seen in a comparable set of local SDSS galaxies, and that [Ne III]/[O III] is enhanced by ~ 0.2 dex. We consider the possible explanations for this $\sim 4\,\sigma$ result, including higher oxygen depletion out of the gas-phase, denser H II regions, higher production of ^{22}Ne via Wolf-Rayet stars, and the existence of a larger population of X-ray obscured AGN at $z \sim 2$ compared to $z \sim 0$. None of these simple scenarios, alone, are favored to explain the observed line ratios. We conclude by suggesting several avenues of future observations to further explore the mystery of enhanced [Ne III] emission.

1. INTRODUCTION

The coupling of multi-object, near-infrared spectrographs to ground-based 8-m class telescopes and the *Hubble Space Telescope* has revolutionized our ability to probe the conditions of star formation in the high-redshift universe. The reason for this is simple: at $z \sim 2$, all the key diagnostic emission lines for density, temperature, and ionization state are shifted into the near-IR, where atmospheric opacity and OH emission severely restrict our ability to measure faint lines. Consequently, virtually all the information we have about the physics of high-z star formation is based upon measurements of the bright lines of hydrogen (Hα and Hβ), oxygen ([O II] λ3727 and [O III] λ5007), nitrogen ([N II] λ6584), and sulfur ([S II] $\lambda\lambda$6717, 6731). Galaxies at $z \sim 2$ have lower oxygen abundances (e.g., Erb et al. 2006), higher ionization parameters (e.g., Nakajima & Ouchi 2014), and harder ionization fields (Steidel et al. 2014) than $z \sim 0$ galaxies with similar stellar mass. Moreover, by using a sample of 14 star-forming galaxies, Shirazi et al. (2014) showed that, for a fixed stellar mass and specific star formation rate, the warm ionized gas in $z \sim 3$ star-forming regions is denser than at $z \sim 0.1$ by a full order of magnitude.

There is, however, one additional bright line that is rarely exploited. [Ne III] λ3869 is the isoelectronic equivalent of [O III] λ5007, with a strength that is often comparable to Hβ. As both neon and oxygen are α-process elements that are produced together in the same regions of Type II supernovae, their abundance ratio should be fixed across population metallicity (Woosley & Weaver 1995; Timmes et al. 1995), and indeed, that appears to be the case locally (Henry 1989; Izotov et al. 2006, 2011). However, Ne^{++} has a slightly higher ionization potential than O^{++} (41.0 versus 35.1 eV), and its principal emission line at 3869 Å has a slightly higher excitation energy (3.2 versus 2.5 eV) and a much higher critical density for de-excitation ($\sim 10^7$ versus 10^6 cm^{-3}) than its oxygen counterpart. The line therefore has significant diagnostic value, and can be used to constrain the conditions of high-redshift star formation (Levesque & Richardson 2014).

There have been few measurements of [Ne III] λ3869 in the high-redshift universe. Perhaps the most detailed is that by Masters et al. (2014), who used co-added spectra to show that for $z = 1.3$ and $z = 2.3$ galaxies, [Ne III] traces [O III] with a strength that is similar but perhaps elevated ($\sim 2\,\sigma$ offset) over that seen in the local universe. The sample size of this program was small (23 galaxies), however, and the diagnostic value of neon was not investigated.

Here we use near-IR spectroscopy from the *Hubble Space Telescope (HST)* and a wealth of ancillary photometric data to examine the emission line ratios of [O III]/Hβ, [Ne III]/[O II], and [Ne III]/[O III] in 236 star-forming galaxies in the redshift range $1.90 < z < 2.35$. In §2, we discuss the data acquired over a ~ 350 arcmin^2 region of the GOODS-N, GOODS-S, and COSMOS fields, and the processing techniques needed to measure individual emission line ratios. In §3, we describe the procedures used to identify a complete, [O III]-selected sample of $z \sim 2$ galaxies, place our sample in the context of other $z \sim 2$ surveys, and identify local systems with similar stellar masses and star formation rates. In §4, we present our measurements of [Ne III] λ3869 with respect to [O II] λ3727, [O III] λ5007, and Hβ. Since only $\sim 25\%$ of our sample have all four lines detected with a signal-to-noise ratio greater than one, we also present measurements of a set of stacked spectra. In this section, we compare our data to neon and oxygen measurements at $z \sim 0$, and demonstrate that the average [Ne III]/[O III] ratio measured at $z \sim 2$ is significantly greater than that seen locally. In §5, we discuss the possible sources of the high [Ne III]/[O III] ratio, including clumpy HII regions, hotter exciting stars, oxygen depletion out of the gas-phase, higher neon to oxygen abundances, and the existence of Compton-thick active

[1] Department of Astronomy & Astrophysics, The Pennsylvania State University, University Park, PA 16802
[2] Institute for Gravitation and the Cosmos, The Pennsylvania State University, University Park, PA 16802
[3] Hubble Fellow

galactic nuclei. We conclude by considering observations which would test these hypotheses.

For this work we adopt a standard ΛCDM cosmology, with $\Omega_M = 0.3$, $\Omega_\Lambda = 0.7$, and $H_0 = 70$ km s^{-1} Mpc^{-1}, and a Kroupa (2001) initial mass function (IMF). Unless stated otherwise, the equivalent widths (EW) discussed in this paper are quoted in the rest-frame.

2. DATA AND REDUCTIONS

Our study of emission line ratios in the $z \sim 2$ universe is focused on three ~ 115 arcmin^2 patches of sky in the COSMOS (Scoville et al. 2007), GOODS-N, and GOODS-S (Giavalisco et al. 2004) fields. These regions have a wealth of photometric and spectroscopic data available for analysis, including broadband photometry from *HST* and *Spitzer*, broad- and intermediate-band photometry from the ground, and optical and near-IR slitless spectroscopy from *HST*.

2.1. *HST Spectroscopy*

Our rest-frame optical emission-line measurements come from the 3D-HST (GO-12177, 12328; P.I. P. van Dokkum) and AGHAST (GO-11600; P.I. B. Weiner) near-IR grism surveys with the WFC3 camera of the *Hubble Space Telescope* (Brammer et al. 2012; Weiner & AGHAST Team 2014). The primary observations of these programs consisted of G141 slitless grism spectroscopy covering the wavelength range $1.08\ \mu\text{m} < \lambda < 1.68\ \mu$m at $R = 130$ resolution with a $0\farcs128$ spatial pixel scale. Approximately 625 arcmin^2 was observed in the course of these surveys, including $\sim 80\%$ of the CANDELS footprint (Grogin et al. 2011); when combined with accompanying direct images through the F140W filter of WFC3, these data provide full coverage of the rest-frame wavelengths 3700-5020 Å for all $1.90 < z < 2.35$ galaxies with unobscured emission line fluxes brighter than $\sim 10^{-17}$ ergs cm^{-2} s^{-1}. This wavelength range includes the strong emission lines of [O II] $\lambda3727$, [O III] $\lambda\lambda4959, 5007$, [Ne III] $\lambda\lambda3869, 3960$, and hydrogen (Hβ, Hγ and Hδ).

An in-depth discussion of the reduction of these data can be found in Zeimann et al. (2014), but in brief, each grism observation was accompanied by a shallow ($\sim$ 200 s) F140W exposure, which served to define the position of each object's wavelength zeropoint and spectral trace. These images were combined using the standard procedures of `MultiDrizzle` (Fruchter et al. 2009), co-added with the deeper CANDELS F125W and F160W frames, and processed by SExtractor (Bertin & Arnouts 1996) to produce a master catalog of all objects brighter than $m_{AB} = 26$ and having more than five pixels above a $3\,\sigma$ per pixel detection threshold. Each object's corresponding grism spectrum was obtained using the optimal extraction setting of version 2.3 of `aXe` (Kümmel et al. 2009), as described in the WFC3 Grism Cookbook[4] (see Zeimann et al. 2014). At the conclusion of this process, the program `aXe2web`[5] was used to convert our final list of objects into a webpage containing each object's 2-D and 1-D extracted spectra, its H-band image, and a summary of its properties. This provided an easy and efficient way to maintain quality control and select subsamples of objects for science purposes.

2.2. *Optical/Near-IR Imaging*

To measure the stellar masses and reddenings of our galaxies, we began with the SExtractor-based photometric catalog of Skelton et al. (2014), which starts with deep, co-added F125W + F140W + F160W images from *HST* and then adds in the results of 30 distinct ground- and space-based imaging programs. The result is a homogenous, PSF-matched set of broad- and intermediate-band flux densities covering the wavelength range 0.35 μm to 8.0 μm over the entire region surveyed by the *HST* grism. In the COSMOS field, this dataset contains photometry in 44 separate bandpasses, with measurements from *HST*, *Spitzer*, Subaru, and a host of smaller ground-based telescopes. In GOODS-N, the data come from *HST*, *Spitzer*, Keck, Subaru, and the Mayall telescope, and include 22 different bandpasses, while in GOODS-S, six different telescopes provide flux densities in 40 bandpasses. For $z \sim 2$ systems, these data cover the rest-frame UV through the rest-frame near-IR and allow excellent estimates of stellar mass, under the necessary assumptions about the underlying stellar population (i.e., stellar metallicity, star formation history, and attenuation law).

3. SAMPLE SELECTION AND MEASUREMENTS

Our galaxy sample is nearly identical to that defined by Zeimann et al. (2014), who visually inspected over 50,000 spectra in their program to identify $z \sim 2$ star forming galaxies. These galaxies satisfied three basic criteria:

- A secure redshift between $1.90 < z < 2.35$. In this redshift interval, the emission lines of [O II] $\lambda3727$, [Ne III] $\lambda3869$, Hγ, Hβ, and [O III] $\lambda4959, 5007$ all fall into the range of the G141 grism. To be part of the sample, a galaxy had to have at least two of these lines reliably detected. At the $R = 130$ resolution of the G141 grism, the [O III] doublet is blended, though with a distinctive, easily-identifiable shape (see Figure 1 of Zeimann et al. 2014). A total of 309 unique galaxies were identified through this condition.
- Minimal contamination from field sources. Overlapping spectra are a significant issue in slitless spectroscopy, as the dispersed order of one source frequently overlaps the spectrum of another. To estimate the importance of this effect, Zeimann et al. (2014) used the sizes and magnitudes of every object in the *HST* grism SExtractor catalog to produce a 2-D Gaussian model of every expected spectrum (Kümmel et al. 2009). This procedure identified most of the spectral superpositions, but not all: in particular, the algorithm occasionally missed some regions where the systematics of contamination subtraction dominate the error in the continuum. Consequently, an additional visual inspection was needed to identify those objects where this systematic error was greater than the statistical error of the target spectrum. This criterion eliminated 57 objects from the sample.
- A well-fit spectral energy distribution. As described in §3.1, we obtained masses for our $z \sim 2$ galaxies by fitting their spectral energy distribution to population synthesis models via a Markov-Chain Monte Carlo code. For 16 objects, this procedure did not converge, due either

[4] http://www.stsci.edu/hst/wfc3/analysis/grism_obs/cookbook.html
[5] http://axe.stsci.edu/axe/axe2web.html

to a misidentification of the asymmetric [O III] doublet, or poor broadband photometry. These objects were excluded from our analysis, leaving us with a final sample of 236 galaxies distributed over the GOODS-N, GOODS-S, and COSMOS fields.

To understand the systematics of this sample, Zeimann et al. (2014), simulated a set of model emission-line spectra in the exact same manner as our program data. These artificial sources were randomly drawn from uniform distributions in redshift ($1.90 < z < 2.35$), log metallicity ($7 < 12 + \log(\mathrm{O/H}) < 9$), and log H$\beta$ flux ($-18 < \log F_{\mathrm{H}\beta} < -16$ ergs s^{-1} cm^{-2}), placed on mock grism frames, and "observed" in the exact same manner as the original data. The results of this experiment can be found in Figure 2 of Zeimann et al. (2014). In brief, for the GOODS-N and GOODS-S fields, our 50% and 80% completeness limits for Hβ flux measurements are $\sim 10^{-17}$ ergs s^{-1} cm^{-2} and $\sim 3 \times 10^{-17}$ ergs s^{-1} cm^{-2}, respectively, with little variation with redshift or metallicity. Due to its higher background, the COSMOS limits are shallower by a factor of ~ 1.5 (Brammer et al. 2012).

Emission line fluxes were determined by fitting the continuum of each $z \sim 2$ spectrum with a fourth-order polynomial, while simultaneously fitting Gaussians of a common width to the emission lines of [O II] λ3727, [Ne III] λ3869, Hγ, Hβ, and [O III] λ4959, 5007. Our choice of polynomial was driven by the possible presence of a 4000 Å break in the stellar continuum, though fits using a series of first-order polynomials around each emission line yielded similar results. Also, we did not correct any of our fits for underlying Balmer absorption (Moustakas et al. 2006). In the local universe, typical corrections for Hβ are of the order of ~ 4 Å equivalent width (EW), but this number is a function of both population age and IMF (Groves et al. 2012). As can be seen in Figure 3 of Zeimann et al. (2014), this factor is relatively small compared to the equivalent widths considered here. Indeed, to verify that the effect is minor, we repeated all our analyses while adding 4 Å EW to each of our Hβ measurements. This action has the effect of increasing all our Hβ fluxes by an average of $\sim 10\%$, hence lowering our [O III]/Hβ ratios by the same amount.

3.1. *Global Properties of the Sample*

To place our neon measurements in context, we must first define the global properties of our galaxy sample, particularly their star formation rates (SFRs) and stellar masses. The former parameter can be computed in two ways: through the Hβ line luminosity, which measures the ionizing flux from $M > 15 M_{\odot}$ stars born in the past $\sim 10^7$ yr, and the rest-frame UV continuum, which records stellar emission from $M > 5 M_{\odot}$ stars younger than $\sim 10^8$ yr (Kennicutt & Evans 2012). Zeimann et al. (2014) investigated the behavior of these two indicators in the same sample of galaxies considered here, and found that UV-based SFRs are less sensitive to shifts in galactic metallicity than Balmer emission. We therefore adopted the Zeimann et al. (2014) UV-based SFRs for our analysis. These values are derived from the photometry of Skelton et al. (2014), and are based on the fits to the 1600 Å flux density, assuming a power-law slope to the UV continuum, the Calzetti (2001) obscuration law, and the local SFR calibration (Hao et al. 2011; Murphy et al. 2011; Kennicutt & Evans 2012).

Our stellar masses are based upon the analysis of Gebhardt et al. (2014), who used the Markov Chain Monte Carlo code GalMC (Acquaviva et al. 2011) to model the spectral energy distribution (SED) of every galaxy in our sample. In brief, the Skelton et al. (2014) photometric measurements were fit to the 2007 version of population synthesis models of Bruzual & Charlot (2003), using a Kroupa (2001) IMF over the range $0.1\,M_{\odot} < M < 100\,M_{\odot}$, a Calzetti (2001) obscuration law, and the prescription for emission lines given by Acquaviva et al. (2011), as updated by Acquaviva et al. (2012). Since stellar abundances are poorly constrained by broadband SED measurements, the metallicity of these models was fixed at $Z = 0.2\,Z_{\odot}$, which is close to the median gas-phase metallicity of our sample (Gebhardt et al. 2014). To avoid the emission from polycyclic aromatic hydrocarbons, all data points redward of rest-frame 3.3 μm were excluded from the fits (Tielens 2008), as were measurements blueward of 1216 Å, where the statistical correction for intervening Lyα absorption (Madau 1995) may not always be appropriate. Finally, for simplicity, the SFR of each galaxy was assumed to be constant with time. Although almost certainly not the case, this constraint does not strongly affect our estimates for the stellar mass.

Figure 1 compares the masses and SFRs of our galaxies to other members of the $z \sim 2$ "galaxy zoo". For the figure, literature SFRs and stellar masses were converted from a Salpeter (1955) IMF to a Kroupa (2001) IMF by subtracting 0.16 and 0.25 dex, respectively. No correction was made from a Chabrier (2003) IMF to a Kroupa (2001) IMF as this correction is small ($\lesssim$6%). We highlight other $z \sim 2$ galaxy samples using ellipses defined to include $\sim 90\%$ of their galaxies. In general, the galaxies selected by the *HST* grism are less massive and have lower star formation rates than systems selected via their broadband continuum measurements. In this respect, our emission-line galaxies are similar to Lyα emitting systems (LAEs, Vargas et al. 2014; Hagen et al. 2014), and, like LAEs, the *HST* emission-line sources tend to fall above the extrapolated SFR-stellar mass "main sequence" defined by Rodighiero et al. (2011).

Another way to view the global properties of our sample of $z \sim 2$ grism galaxies is through a comparison with local star-forming systems. Such an analysis is not straightforward since, on average, $z \sim 2$ systems form stars ten times more rapidly than do local objects (e.g., Whitaker et al. 2014). Nevertheless, we can create an analogous sample by applying luminosity, equivalent width, and stellar mass cuts to the Sloan Digital Sky Survey (SDSS; York et al. 2000) Data Release 7 (Abazajian et al. 2009) MPA-JHU galaxy catalog[6]. Specifically, we selected objects with extinction-corrected Hβ luminosities $L_{\mathrm{H}\beta} \geq 3 \times 10^{40}$ ergs s^{-1}, stellar masses between $7.5 < \log(M/M_{\odot}) < 11.5$, and H$\beta$ equivalent widths greater than 5 Å (so that the measurement of flux is not dominated by the correction for stellar absorption). For inclusion in our comparison sample, we also required that the galaxies' emission line fluxes at [O II] λ3727, [Ne III] λ3869, Hβ, [O III] λ5007, and [O III] λ4363 all be

[6] www.mpa-garching.mpg.de/SDSS/DR7

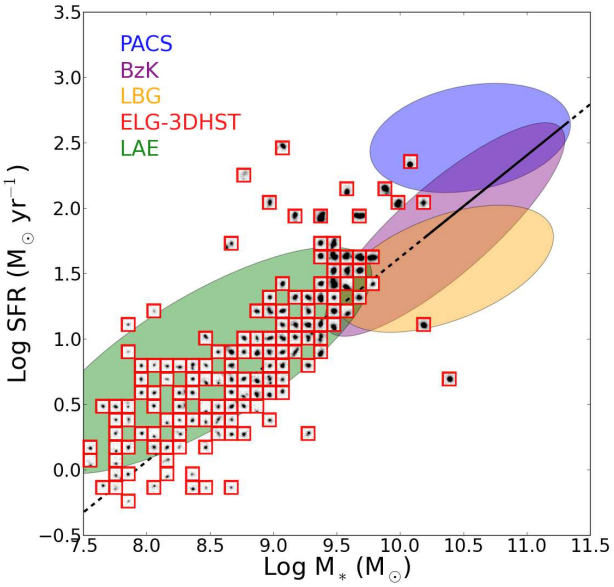

FIG. 1.— A sample of our $z \sim 2$ star forming galaxies in the context of the epoch's "galaxy zoo". The position of each F160W cut-out shows the system's stellar mass and star formation rate, as derived from its spectral energy distribution (Skelton et al. 2014). These "normal" emission-line galaxies have lower stellar masses and star formation rates than $z \sim 2$ systems selected via their *Herschel* sub-mm emission (blue PACS galaxies; Rodighiero et al. 2011), Lyman break (yellow galaxies; Erb et al. 2006), or optical/IR colors (purple *BzK* galaxies; Rodighiero et al. 2011). In this respect, they are similar to Lyα emitting galaxies (green LAEs; Vargas et al. 2014; Hagen et al. 2014). The solid black line is the star-forming "main sequence" of Rodighiero et al. (2011), while the dashed line extrapolates this relation.

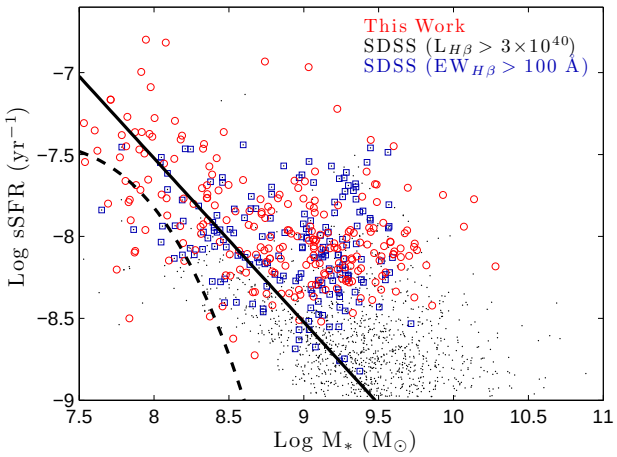

FIG. 2.— The mass-specific star formation rate versus stellar mass diagram for our $z \sim 2$ grism galaxies (red open circles) and a local comparison sample from SDSS (black dots). The blue open squares identify the subset of local galaxies with high Hβ equivalent widths. The black solid line illustrates our 50% Hβ flux limit converted into a rest-frame UV-based SFR at $z \sim 2.1$, using a Kroupa (2001) IMF and the $Z = 0.2Z_\odot$ metallicity correction suggested by Zeimann et al. (2014). The dashed black curve corresponds to our completeness limit (F140W = 26) for a 2007 Bruzual & Charlot (2003) stellar population model with $Z = 0.2Z_\odot$ and a constant star formation history. The closest local analogs to our emission-line galaxies at $z \sim 2$ are the high-equivalent width objects studied by Izotov et al. (2011).

at least twice as large as their flux error. This latter criterion facilitated direct measurements of the systems' electron temperatures, enabling a better understanding of their physical conditions (Osterbrock & Ferland 2006), while only reducing the sample by $\sim 20\%$.

Our selection criteria resulted in the identification 2890 galaxies between $0.02 < z < 0.40$ with a median redshift of $z \sim 0.12$. As illustrated in Figure 2, our $z \sim 2$ grism galaxies have mass-specific star formation rates that are much higher than most of the comparison objects. Consequently, to obtain an even better set of analogs, we further restricted the local sample to "young" galaxies, i.e., systems with high Hβ equivalent widths (EW$_{\rm H\beta}$ > 100 Å). As Figure 2 demonstrates, this additional criterion creates a local sample that is quite similar to our $z \sim 2$ dataset, i.e., the distant star-forming galaxies identified by the *HST* grism are comparable in both mass and specific star formation rate to the "green pea" galaxies (Cardamone et al. 2009) and the luminous blue compact galaxies identified by Izotov et al. (2011) in their analysis of the SDSS spectral catalog. By including lower equivalent width objects in our initial sample, however, we did diversify the population: as the commonly used Baldwin et al. (1981) diagnostic indicates, the larger comparison set contains both star forming regions and AGN, with some objects being composites of the two populations. This information will be useful for our subsequent analysis.

4. THE NEON-OXYGEN LINE RATIOS

Figure 3 plots the [O III]/Hβ, [Ne III]/[O II], and [Ne III]/[O III] line ratios against stellar mass for our sample of $z \sim 2$ star-forming galaxies, the Steidel et al. (2014) sample of massive ($9 \lesssim \log {\rm M_*/M_\odot} \lesssim 11.5$) $z \sim 2.3$ star-forming ($0.5 \lesssim \log {\rm SFR\ (M_\odot\ yr^{-1})} \lesssim 2$) galaxies, and our more inclusive local comparison sample. To illustrate the sequences, the local systems have been color-coded by their [O III] λ4959 + 5007 / [O III] λ4363 electron temperature (Osterbrock & Ferland 2006), and AGN-dominated systems, as determined by the mass-excitation diagnostic (Juneau et al. 2011, 2014), have been plotted in black. From the figure, it is clear that, although the measurement uncertainties are large, our $z \sim 2$ star-forming galaxies have neon/oxygen line ratios that are significantly higher than that seen in the local universe. In the [Ne III]/[O II] diagram, the *HST* grism galaxies typically lie $\sim$ 0.2 dex above the sequence defined by local starbursting galaxies, while for [Ne III]/[O III], the median offset is ~ 0.3 dex. We note that, unlike the [O III]/Hβ and [Ne III]/[O II] line ratios, the [Ne III]/[O III] diagnostic is sensitive to reddening. However, extinction corrections will only make the discrepancy worse by boosting [Ne III] relative to [O III]; if we convert the UV-based stellar reddenings into nebular extinctions via the obscuration law of Calzetti (2001), the median offset increases to $\sim$ 0.4 dex. These high neon/oxygen ratios stand in striking contrast to the results from [O III]/Hβ, where the values for this index are well-matched for metal-poor $z \sim 0$ analogs with high electron temperatures. Whatever is causing neon to appear enhanced is not changing the expected strength of [O III] λ5007.

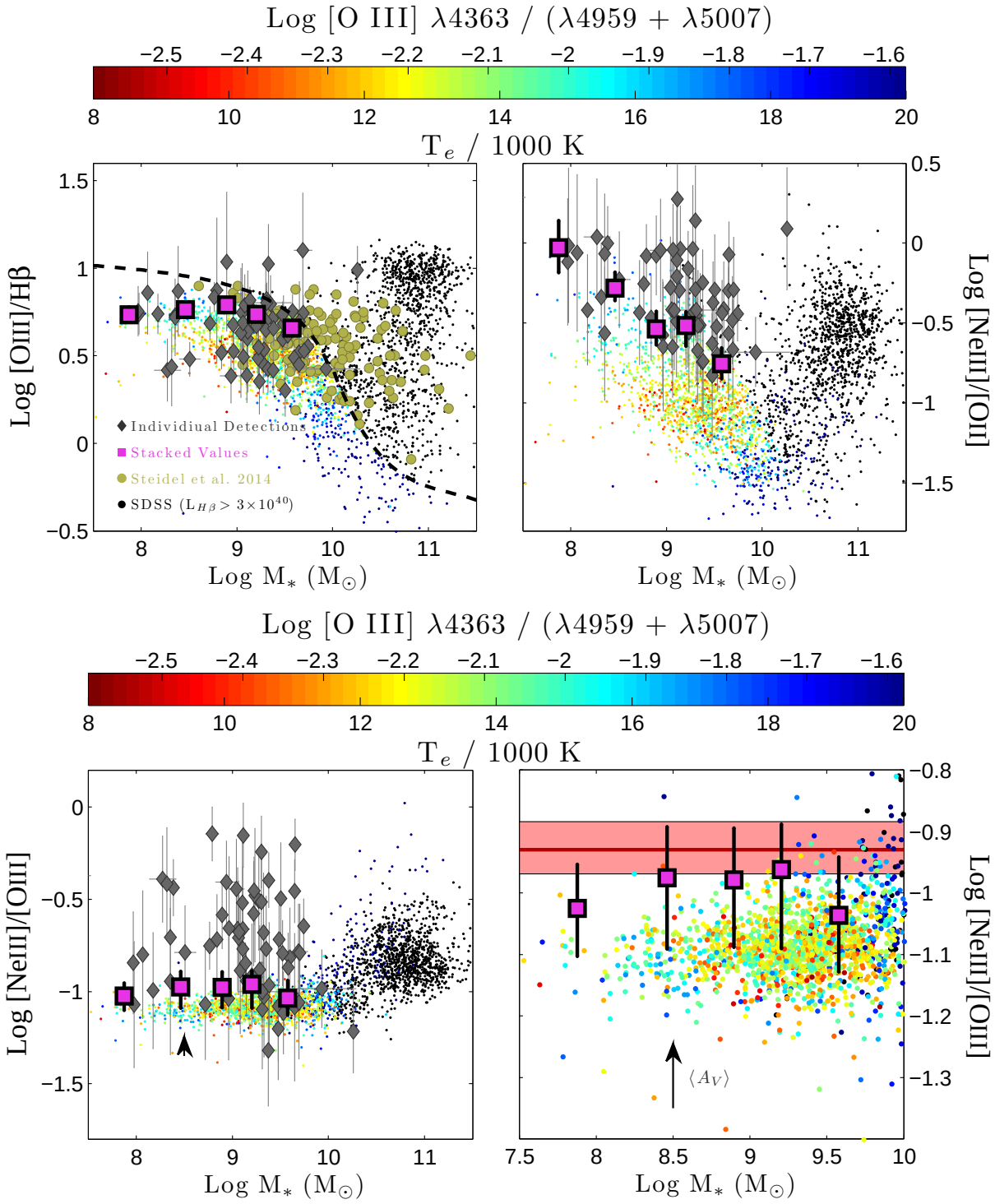
Log [O III] λ4363 / (λ4959 + λ5007)
−2.5 −2.4 −2.3 −2.2 −2.1 −2 −1.9 −1.8 −1.7 −1.6
8 10 12 14 16 18 20
T_e / 1000 K
Log [OIII]/Hβ
Log [NeIII]/[OII]
Individiual Detections
Stacked Values
Steidel et al. 2014
SDSS (L_Hβ > 3×10^40)
Log M* (M⊙)
Log [O III] λ4363 / (λ4959 + λ5007)
−2.5 −2.4 −2.3 −2.2 −2.1 −2 −1.9 −1.8 −1.7 −1.6
8 10 12 14 16 18 20
T_e / 1000 K
Log [NeIII]/[OIII]
Log [NeIII]/[OIII]
⟨A_V⟩
Log M* (M⊙)
Log M* (M⊙)

FIG. 3.— The observed ratios of [O III]/Hβ (top left), [Ne III]/[O II] (top right), and [Ne III]/[O III] (bottom left) as a function of stellar mass, as derived from SEDs. The small dots show the more inclusive sample of local SDSS galaxies, color-coded by their [O III]-based electron temperature, going from T_e = 8000 K (red) to 20000 K (blue), with black representing AGN-dominated systems (Juneau et al. 2014). The grey diamonds show the $z \sim 2$ *HST*-grism galaxies with secure [Ne III] detections (along with their 1 σ error bars), while the purple squares denote values obtained from our median stacks (which include non-detections). The error bars for the stacks are the 16$^{\rm th}$ and 84$^{\rm th}$ percentiles of 500 bootstrap with replacement iterations. In the [O III]/Hβ diagram, we have also added measurements from the Steidel et al. (2014) survey of more massive galaxies at $z \sim 2.3$ (gold dots), and have illustrated the dividing line between star-forming and AGN-dominated systems, as estimated from the MEx diagnostic for $z \sim 2$ and high-luminosity limits (Juneau et al. 2014). The arrow on the [Ne III]/[O III] diagram represents the median extinction correction, based on the galaxies' UV slopes and a Calzetti (2001) obscuration law. The bottom right panel is an expanded version of the [Ne III]/[O III] diagram, where the individual $z \sim 2$ measurements have been replaced with their median value (red line), and their 16$^{\rm th}$ and 84$^{\rm th}$ percentiles (light red band). [Ne III] λ3869 is consistently brighter than expected from local samples.

4.1. *Stacked Measurements*

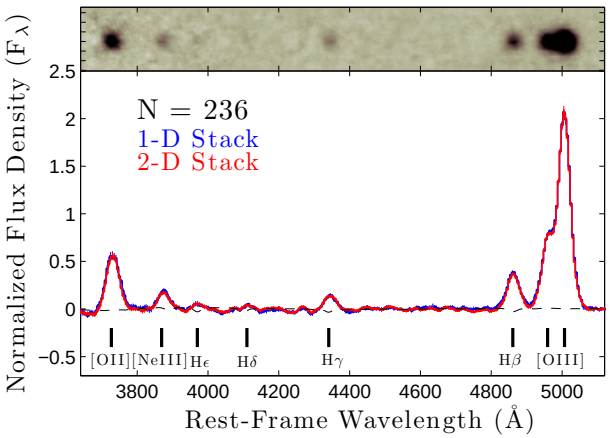

FIG. 4.— The top panel shows the observed median 2-D spectrum of our entire $z \sim 2$ galaxy sample, with black indicating higher intensity. The bottom panel compares the observed spectrum obtained by summing the central ±3 pixels of this image (red) to that obtained by median combining all the 1-D extracted spectra (blue). The error bars, which are barely visible in this scaling, were calculated using 500 bootstraps with replacement iterations, computing the median values, and taking the 16th and 84th percentiles of each wavelength bin. The spectral resolution of the stacked sample is ∼30 Å. The location of the emission lines of [O III] λ3727, [Ne III] λ3869, [O III] $\lambda\lambda$4959, 5007, and the Balmer series (Hβ, Hγ, Hδ, and Hϵ) are marked. The black dashed curve is the continuum-subtracted stack of the best-fit stellar spectral energy distributions.

In many of our $z \sim 2$ star forming galaxies, [Ne III] λ3869 is too faint to detect, and by omitting these galaxies from our analysis, we are biasing our sample. In fact, only $\sim 25\%$ of our galaxies have [O II], [Ne III], Hβ, and [O III] all measured with a signal-to-noise ratio greater than one. Consequently, to understand the rest of the star-forming population, we must rely on spectral stacks of various galaxy subsets, obtained from both the 1-D extracted spectra and from the original 2-D data.

To perform these stacks, we followed the procedures discussed in Francis et al. (1991). We began by subtracting the continuum from each spectrum using a single fourth-order polynomial in the 1-D case and multiple fourth-order polynomials covering the spatial direction for the 2-D data. We then shifted each spectrum into the rest frame via linear interpolation with 1/3 pixel (5 Å sampling) in the wavelength direction, and 1/3 pixel (0.″04) sampling in the spatial direction. Slightly different sampling sizes (i.e., 1/2 or 3/4 of a pixel) did not substantially effect the result. Next, we scaled each spectrum to its flux in the [O III] λ5007 line, and computed the median value for each wavelength, and (for the 2-D spectral extractions) for each spatial position. By median stacking, we preserved the relative strengths of the emission lines, enabling us to measure line ratios. We then computed errors for the median stack using the 16th and 84th percentiles of 500 bootstrap with replacement iterations of this process. Finally, to check for consistency, we summed the central ±0.″128 (±3 re-sampled pixels, or ∼ 1 kpc) of the 2-D median spectrum and compared it to the corresponding median produced from the 1-D analysis. As Figure 4 illustrates, there is excellent agreement between the two results. The collapsed 2-D median spectrum does have a slightly higher signal-to-noise ratio than the 1-D median, and we use that in the analysis below. However, the results do not change if we use the 1-D median stacks.

To investigate the behavior of [Ne III] λ3869 with galaxy type, we divided our sample of $z \sim 2$ galaxies into subgroups and stacked their spectra by stellar mass, SFR, and mass-specific star formation rate (sSFR) . As expected, the results of these analyses are correlated, since, as can be seen in Figure 1, star formation rate and stellar mass are related. Moreover, as Figure 2 illustrates, our selection criteria produce an artificial correlation between sSFR and stellar mass at the low mass end of our distribution. In what follows, we choose mass as the independent parameter, understanding that for our sample, lower mass galaxies will have, on average, lower SFRs but higher sSFRs.

Table 1 presents the median line ratios for the stacked spectra of five mass bins. These values are displayed via the purple squares in Figures 3, and Figure 5 compares the ratios to measurements of [O III]/Hβ, [Ne III]/[O II], and [Ne III]/[O III] for the well-matched local sample of high Hβ equivalent width objects. From the figures, it is clear that the forbidden neon-to-oxygen line ratios of the $z \sim 2$ universe are offset from those observed in nearby galaxies, even when comparing to systems with identical stellar masses and specific star-formation rates. In the [Ne III]/[O II] diagram, the trend with stellar mass follows that defined by local low-mass starburst galaxies, but with a mean offset of ~ 0.12 dex, which is still marginally consistent with the high-EW$_{H\beta}$ local sample. The offset in the [Ne III]/[O III] diagram is more dramatic: even if one assumes *no* extinction, there is still a $\gtrsim 0.06$ dex offset between the $z \sim 2$ and local sample for each mass bin. If a Calzetti (2001) obscuration law and the UV slope is used to correct each grism spectrum prior to stacking, this offset balloons to $\gtrsim 0.16$ dex across all masses ($7.5 < \log(M_*/M_\odot) < 10.5$). In contrast, there is no difference between the [O III]/Hβ ratios derived from our median stacks and the local galaxies. Table 2 describes these offsets.

5. INTERPRETING THE LINE RATIOS

Although they are likely oversimplified, photoionization models have both qualitatively and quantitatively reproduced the emission line ratios in the local universe (Kewley & Dopita 2002; Dopita et al. 2006). We can therefore use such models (e.g., CLOUDY Version 13.03; Ferland et al. 1998, 2013) to gain insight into the dominant physical parameters which govern emission lines at $z \sim 2$.

To do this, we ran a grid of uniform-density plane-parallel CLOUDY models, fixing the relative elemental abundances at solar values (in particular, $\log \mathrm{Ne/O} = -0.76$), while varying the nebula's oxygen abundance ($-2 < [\mathrm{O/H}] < 0$), electron density ($10 < n_e < 10^6$ cm^{-3}), ionization parameter ($-3.2 < \log U < -1.4$, where U is the ratio of ionizing photons to the number density of atoms), and hardness of the ionizing spectrum ($40,000$ K $< T_{\rm eff} < 70,000$ K). We then examined the strengths of the [Ne III] λ3869, [O II] λ3727, [O III] λ5007, and Hβ lines as a function of these parameters, in

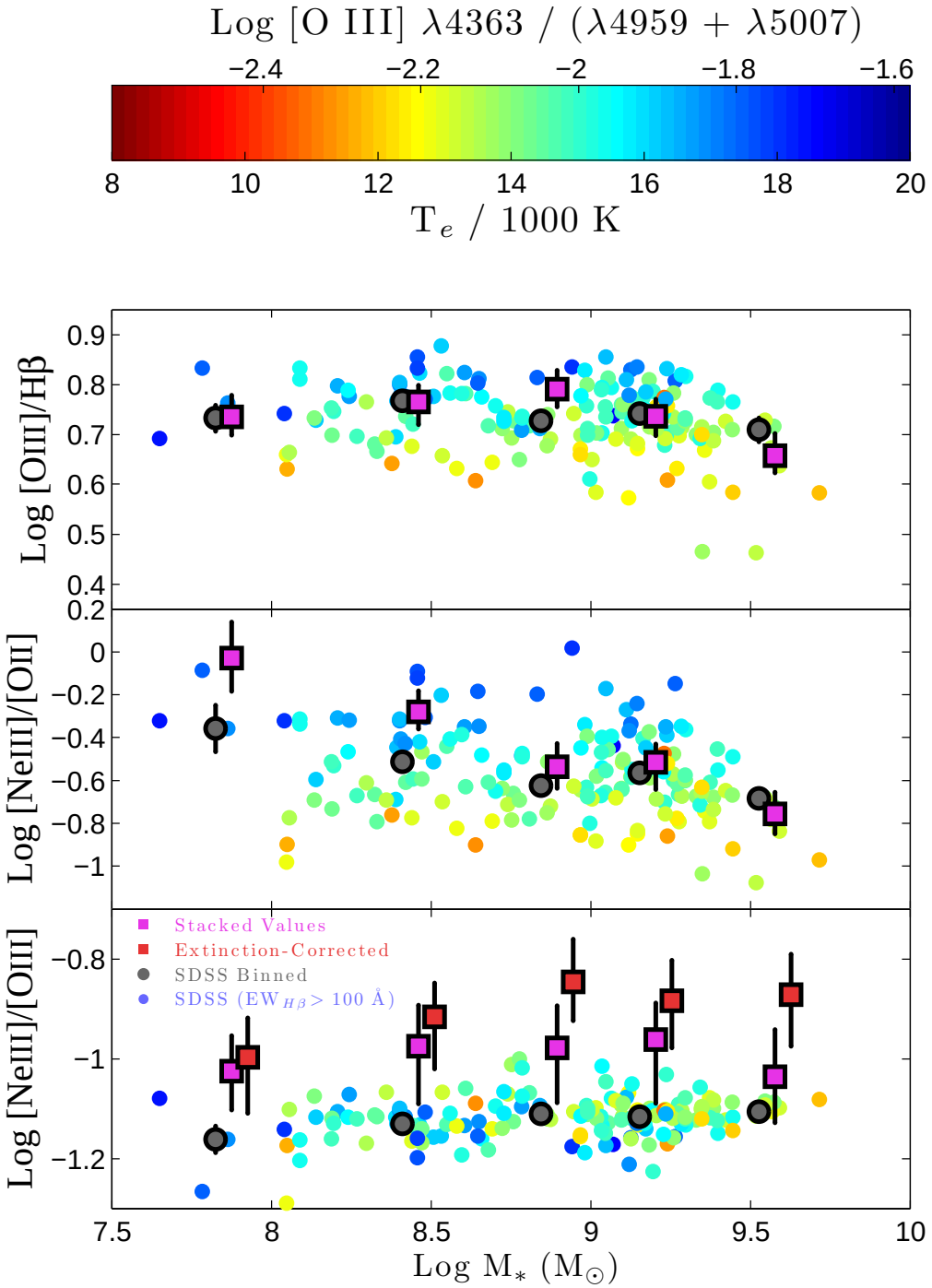

FIG. 5.— The observed ratios of [O III]/Hβ (top), [Ne III]/[O II] (middle), and [Ne III]/[O III] (bottom) as a function of stellar mass, as derived from SEDs. The small dots show the local SDSS comparison galaxies with EW$_{H\beta}$ > 100 Å, color-coded by their [O III]-based electron temperature, from T_e = 8,000 K (red) to 20,000 K (blue). The grey circles are the median values for this sample, with their 1σ uncertainties. The purple squares denote values obtained from our median stacks of $z \sim 2$ systems, while the red squares in the [Ne III]/[O III] diagram use the galaxies' UV slopes and the Calzetti (2001) obscuration law to correct these values for reddening. The error bars are computed as in Figure 3, and only include the statistical uncertainties associated with median stacking. The [Ne III]/[O III] values in our $z \sim 2$ galaxies are consistently higher than expected from local samples.

order to explore the possible origins of enhanced neon-to-oxygen ratios. The local analog sample line ratios are best reproduced by CLOUDY models with densities between 10^2-10^3 cm^{-3}, effective black body temperatures of $55,000$ K $< T_{\rm eff} < 65,000$ K, ionization parameters in the range of $-2.8 < \log U < -2.0$, and oxygen abundances between $8.1 < 12 + \log {\rm O/H} < 8.6$. These values are slightly higher but still consistent with the metallicity range measured via [O III]λ4363 and agree with the best-fit values of the CLOUDY models used by Steidel et al. (2014) for their $z \sim 2.3$ sample.

Our analysis is similar to that performed by Levesque & Richardson (2014), who mated the MAPPINGS III photo-ionization code (Binette et al. 1985; Sutherland & Dopita 1993; Groves et al. 2004) to STARBURST99 (Leitherer et al. 1999; Vázquez & Leitherer 2005) instantaneous burst stellar populations, using the assumption of a plane-parallel isobaric geometry and $n_e = 100$ cm^{-3}. Their results (as seen in their Figure 2), overestimate the local relationship between [Ne III]/[O III] by ~ 0.4 dex, and predict line strengths that are even greater than that seen in the $z \sim 2$ universe. The source of the discrepancy is unknown.

5.1. *Interpretation*

To understand the line ratios displayed in Figures 3 and 5, we begin by considering the local sample of galaxies. In the diagrams, we plot two sets of objects: those whose line ratios suggest the presence of an AGN, and those which appear to be normal star-forming galaxies. The former systems are generally identified by comparing [O III]/Hβ to [N II]/Hα (i.e., via the BPT diagram; Baldwin et al. 1981), although in the absence of [N II]/Hα, stellar mass can be used as a proxy (Juneau et al. 2011, 2014). Few of our objects fall on this AGN sequence; in general, the $z \sim 2$ galaxies detected by the *HST* grism are lower-mass objects with [O III]/Hβ ratios that place them securely in the star-formation region of the diagram. The star-forming galaxies themselves lie on a sequence traced by both the nebular electron temperature and excitation: as the mass of a system decreases, the auroral [O III] λ4363 line becomes more prominent, and the dominant state of oxygen shifts from O^+ to O^{++}. Both of these trends are generally interpreted as being due to metallicity, as fewer metals mean hotter stars and larger ionization parameters (e.g., Massey et al. 2005), while fewer coolants translate into higher electron temperatures (e.g., Evans & Dopita 1985; Dopita et al. 2006).

The [Ne III] line ratios derived from the stacked spectra follow these trends. As the stellar mass and metallicity increase, there is a decline in the (reddening independent) ratio of [Ne III]/[O II] which exactly follows that seen in the local universe. Meanwhile, the (reddening-corrected) [Ne III]/[O III] ratio marginally increases by 0.08 ± 0.05 dex per dex in stellar mass, again, consistent with local observations (0.02 ± 0.02 dex per dex in stellar mass).

The difficulty arises when considering the absolute strength of [Ne III] λ3869. Neon and oxygen are formed together in Type II supernovae (Woosley & Weaver 1995; Timmes et al. 1995), and their doubly-ionized states have similar ionization potentials. Consequently, in the local universe, [Ne III] λ3869 and [O III] λ5007 are tightly correlated across all star-forming galaxies (e.g., Izotov et al. 2006, 2011). The 178 high-equivalent width (EW$_{\rm H\beta} > 100$ Å) starburst galaxies which most closely match our $z \sim 2$ systems in both stellar mass and specific star formation rate are plotted in Figure 2. The median de-reddened value of [Ne III]/[O III] for these objects is 0.078 ± 0.001. In contrast, the value for our total median stacked $z \sim 2$ spectrum is 0.091 ± 0.008 without any correction for reddening. If we then de-redden each spectrum using the slope of the stellar UV continuum and a Calzetti (2001) obscuration law, the ratio of the re-stacked data becomes 0.118 ± 0.011, i.e., nearly $4\,\sigma$ greater than the local measurement. This offset is higher than that found by Masters et al. (2014), who obtained a $\sim 2\,\sigma$ offset of 0.085 ± 0.003 using the extinction-corrected composite spectrum of 23 galaxies with $8.5 < \log(M/M_\odot) < 9.5$ and $\langle z \rangle \sim 1.8$. Masters et al. (2014) did note, however, that their data have a rather large ($\sim 20\%$) uncertainty in the relative calibration of [O III] to Hα. Their measurements are therefore consistent with ours when taking the relative calibration uncertainties into account.

The $\sim$1.5$\times$ enhancement in the [Ne III] emission of $z \sim 2$ star-forming galaxies over that seen in local galaxies with similar global properties, has several possible explanations:

5.1.1. *Potential Systematics*

The high [Ne III]/[O III] ratio found for our $z \sim 2$ galaxies relies on our stacking analysis, so an error in our methodology or extinction correction could result in an elevated ratio. To investigate the former, we scrutinized the flux calibration, continuum subtraction, and biases related to our stacking methodology. For flux calibration, we relied only on the G141 grism calibration[7], which has been documented to be accurate to $\leq 5\%$. Nevertheless, to test the relative flux calibration over scales of $\sim$2000 Å, we binned our data by redshift (or, equivalently, by observed wavelength) and found no significant variations in the ratios of emission line strengths, suggesting that the flux calibration is indeed stable. Similarly, to test for errors in our continuum subtraction, we binned our data by estimated levels of spectral contamination. In our 1-D and 2-D grism spectra, the underlying continuum is a combination of stellar emission from the galaxy and residual contamination from overlapping spectra (see Section 3.1). To capture the trends in both, we fit the continuum with a fourth order polynomial, and this could, in theory, introduce a systematic bias. However, an analysis of our spectra shows no significant relation between line strength and contamination. Moreover, when we repeated our stacking procedure using the best-fit SEDs from our stellar mass estimations, the simplified polynomial approximation enhanced [Ne III] (by 5%), leaving [O II] and [O III] relatively unaffected.

To verify the robustness of our stacking procedure, we compared the line ratios found from the median stacks of all the objects with individual line detections with the median of the individual line ratios measured from these same data. The results were consistent. Also, to examine whether our extinction corrections were affecting the

[7] www.stsci.edu/hst/wfc3/documents/ISRs/WFC3-2011-05.pdf and www.stsci.edu/hst/wfc3/documents/ISRs/WFC3-2014-01.pdf

stacking process, we compared the results of stacks where reddening corrections were applied prior to stacking with similar stacks where de-reddening occurred only after the fact. Again, there was no difference in the results. Finally, one complication related to WFC3 IR grism extractions is that the point spread function (PSF) becomes slightly larger with wavelength. For point sources this must be taken into account, but if the galaxies are substantially larger than the PSF, the issue is mitigated. As seen in the cutouts of Figure 1, most of our $z \sim 2$ galaxies are indeed resolved. An examination of the spatial dependence of our 2-D stacked spectra confirms that the extraction algorithm is not introducing a significant systematic error into our line measurements: the spatial extent of [O II] and [O III], the two emission lines with the largest wavelength separation, are consistent ($\sim 0\farcs49$ full-width half maximum for the total stack).

The significance of our [Ne III]/[O III] result also depends on how we correct our spectra for the effects of dust. Due to the excellent photometric coverage in the rest-frame UV, the uncertainties associated with our stellar reddenings are relatively small, and this term contributes only $\sim$ 30% of the total [Ne III]/[O III] error budget. However, the possible systematic uncertainty associated with our nebular extinctions could be larger. To translate our stellar reddenings into nebular extinctions, we used the Calzetti (2001) obscuration law, which states that the applicable extinction for nebular lines is greater than that for starlight by $E(B-V)_{\rm stars} = 0.44E(B-V)_{\rm gas}$. This result is supported by numerous comparisons of UV- and Balmer line-based SFR measurements in the $z \gtrsim 2$ universe (Förster Schreiber et al. 2009; Mannucci et al. 2009; Wuyts et al. 2013; Price et al. 2014; Holden et al. 2014; Zeimann et al. 2014), but counter-examples exist as well (Erb et al. 2006). Thus, we can take the very conservative approach and assume that the stars and gas are equally extinguished. Under this prescription, the ratio of [Ne III]/[O III], 0.107 ± 0.010, is still discrepant with the local value at the $\sim 3\,\sigma$ level. It is therefore exceedingly unlikely that the high neon ratios seen at $z \sim 2$ are due to our assumptions about reddening.

5.1.2. *Collisional De-Excitation*

The critical density of the $2P\ ^1D_2$ state of O^{++} that produces [O III] λ5007 is $\sim 10^6$ cm^{-3}; for the equivalent state of Ne^{++}, this density is $\sim 10^7$ cm^{-3}. Hence if the density of a typical $z \sim 2$ H II region is significantly greater than that observed for H II regions in the local universe (i.e., $n_e \gtrsim 10^5$ cm^{-3}), collisional de-excitation of oxygen will cause [Ne III] λ3869 to appear enhanced. Such densities are more extreme than what is usually seen in massive $z \sim 3$ galaxies (Shirazi et al. 2014), but are still plausible, especially if the star-forming regions follow a size-density relation (e.g., Kennicutt 1984; Hunt & Hirashita 2009). Moreover, high densities have been invoked to explain the strengths of mid-infrared emisson lines in the Antennae galaxies (Snijders et al. 2007), as well as the emission from the molecular gas of ultra-luminous infrared galaxies (Solomon et al. 1992). The effect of electron density on our line ratios can be seen in Figure 6. We display, from left to right, the three projections of our three dimensional emission-line space and overlay our CLOUDY models for three different densities: 10, 10^3, 10^5 cm^{-3}. For this analysis, the ionizing spectrum has been fixed to a 55,000 K blackbody spectrum as suggested in Steidel et al. (2014). The figure demonstrates that densities of $\lesssim 10^3$ cm^{-3} can successfully explain the line ratios of local galaxies, with perhaps a small deficit of [O III]. However, no value of abundance, ionization parameter, or density can simultaneously explain all three line ratios for the $z \sim 2$ systems.

The difficulty with invoking high densities is that the collisional de-excitation of oxygen should affect other lines as well. For example, if [O III] emission were decreased by the requisite $\sim$ 50%, the [O III]/Hβ ratio would be lowered by that same factor. This decrease is not evident in the top left panel of Figure 3. Similarly, because the critical density for the nebular lines of [O II] is $\sim 10^3$ cm^{-3}, the [Ne III]/[O II] ratio would be *greatly* enhanced in a high-density environment (by at least a factor of $\sim$ 5; see Figure 6). While it may be possible to design a multi-zone model wherein [O II] and [O III] are produced in different regions of a galaxy, substantial tuning would be needed, and the [O III]/Hβ discrepancy would remain.

5.1.3. *Hotter Exciting Stars*

For more than a decade, it has been clear that high-redshift galaxies have, on average, higher [O III]/Hβ ratios than similar galaxies in the local universe (e.g., Teplitz et al. 2000). With the largest sample of $z \sim 2.3$ galaxies observed to date, Steidel et al. (2014) showed that, at any given [N II]/Hα, higher than normal [O III]/Hβ ratios could be obtained by increasing the temperature of the ionizing source from the assumed value of $\sim 42,000$ K for the local SDSS galaxies, to $\sim 55,000$ K. Since Ne^{++} has a higher ionization potential than O^{++}, this change could, in theory, increase the fraction of doubly-ionized neon relative to oxygen. However, the difference in the ionization potentials of the two species is only 5.9 eV (41.0 eV versus 35.1 eV), so once beyond 45,000 K, increasing the temperature of a blackbody source has little effect on the ratio of the ionization states. This result is illustrated in Figure 7.

Galaxies, of course, are not a single blackbody sources, but a composite of many different stars with different effective temperatures. To examine this effect, we used the STARBURST99 (SB99, version 6.0.4) population synthesis code (Leitherer et al. 1999; Vázquez & Leitherer 2005) to create a more realistic ionizing spectrum for CLOUDY input. For a constant star formation history, the ionizing spectrum of a SB99 galaxy is insensitive to age, once the system is older than $\sim 10^7$ yr. Indeed, if all the other parameters are fixed, the ionizing spectrum is well-fit by a blackbody with an effective temperature primarily determined by the stellar metallicity. For a $Z = 0.02Z_\odot$ system, this temperature is roughly 65,000 K; for $Z = 0.2Z_\odot$, it is 55,000 K, and varying the high-mass slope of the IMF has little effect on this result. We did not explore binary population synthesis or the effects of stellar rotation, but it is clear that standard SB99 models cannot produce a spectrum that is hard enough to match the observed line ratios.

5.1.4. *Oxygen Depletion Onto Dust Grains*

While neon is an inert gas, oxygen is reactive, and can be depleted out of the gas phase onto dust grains

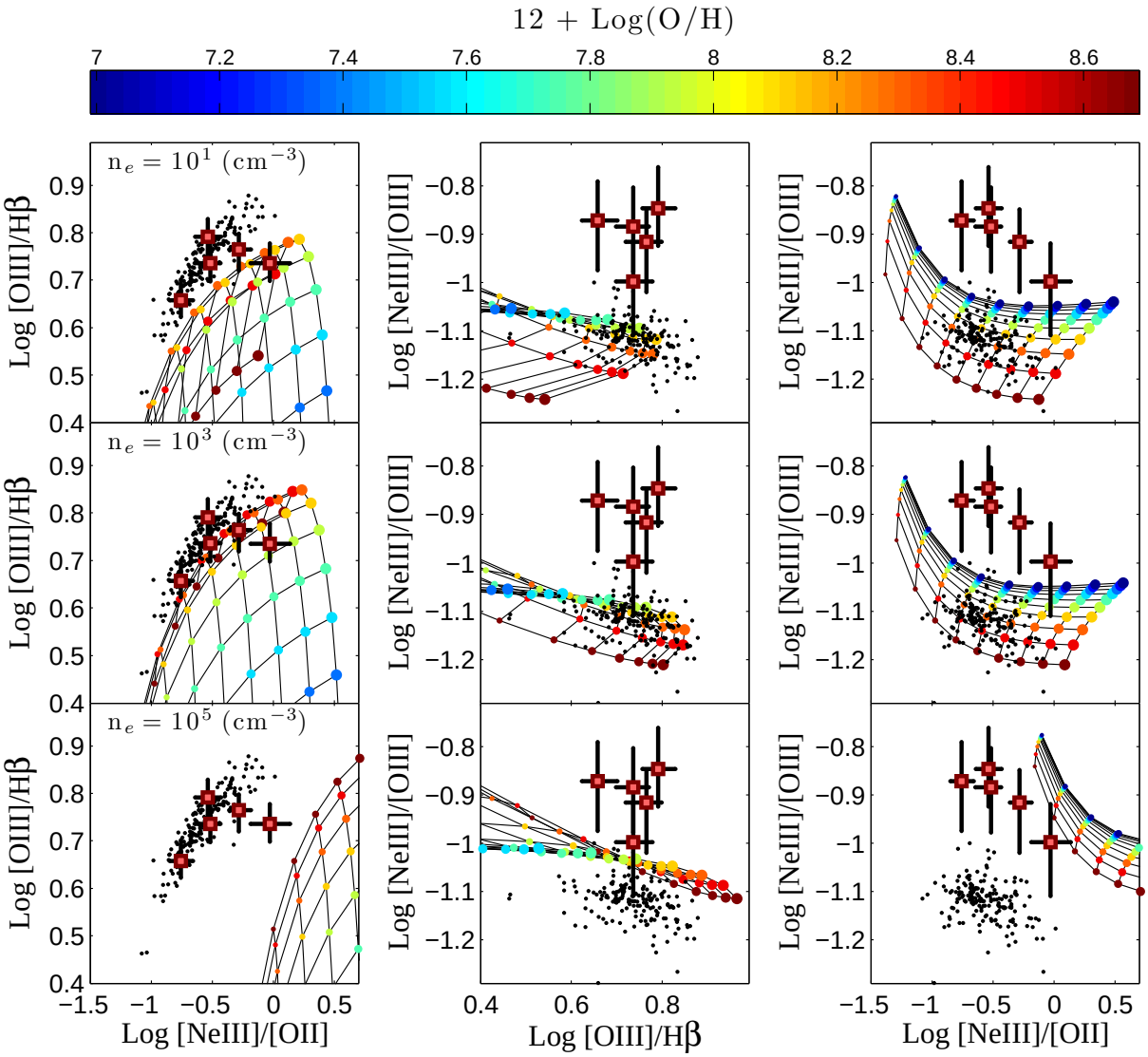

FIG. 6.— The line ratios of our high Hβ equivalent width local galaxies (black dots) and our stacks of $z \sim 2$ emission-line galaxies (red squares) compared to the predictions of CLOUDY models in three different projections of our emission-line space. [Ne III]/[O III] has been corrected for extinction using the Calzetti (2001) obscuration law. The points on the CLOUDY grid are color-coded by metallicity following the scale at the top of the diagram, with the size of each point proportional to the value of the ionization parameter. The temperature of the ionizing source has been held fixed at 55,000 K. From top to bottom the grids represent densities of 10, 10^3, and 10^5 cm^{-3}. Although the lower density models can reproduce the line ratios of the local galaxies reasonably well, no model can fit the $z \sim 2$ data.

or molecules. In the local universe, $\sim 40\%$ of oxygen is thought to be locked up in grains and molecules such as water and O_2 (Jenkins 2009); if this ratio is higher in the $z \sim 2$ universe, then our [Ne III] λ3869 observations can be explained. However, one expects fewer opportunities for dust depletion at $z \gtrsim 2$, not more. Conventionally, oxygen is bound up by refractory compounds such as metallic oxides and amorphous silicates, which require the prior existence of α-process and iron-peak elements. In the metal-poor environment of our $z \sim 2$ systems, this process must be inhibited. On the other hand, when oxygen consumption is measured against the abundance of metals such as Mg, Si, and Fe, its depletion from the gas phase is six times higher than expected (Jenkins 2009). This suggests the existence of an additional avenue for the removal of oxygen from the gas phase. However, since this second avenue probably involves the creation of ices on the surfaces of dust grains (Ioppolo et al. 2008), it is still likely to depend on metallicity. Still, the possibility of dust depletion cannot be ruled out.

5.1.5. *Enhanced Neon to Oxygen Abundance*

The most straightforward interpretation is that the neon to oxygen abundance ratio in the $z \sim 2$ universe is enhanced by ~ 0.2 dex over that of the local universe. At face value, this scenario seems unlikely. In the Sun, the dominant isotope of neon is that of ^{20}Ne, which contributes 92.9% of all neon atoms, with ^{22}Ne being the next most abundant species (6.8%; Asplund et al. 2009). Since ^{20}Ne is formed directly from ^{16}O via α-capture, the formation regions of the two species must be highly correlated. Indeed, abundance measurements in Milky Way and Magellanic Cloud planetary nebulae (Henry 1989), H II regions (Garnett 2002), and other galaxies (Izotov et al. 2006, 2011) yield the same cosmic Ne/O abundance over a wide range of metallicity

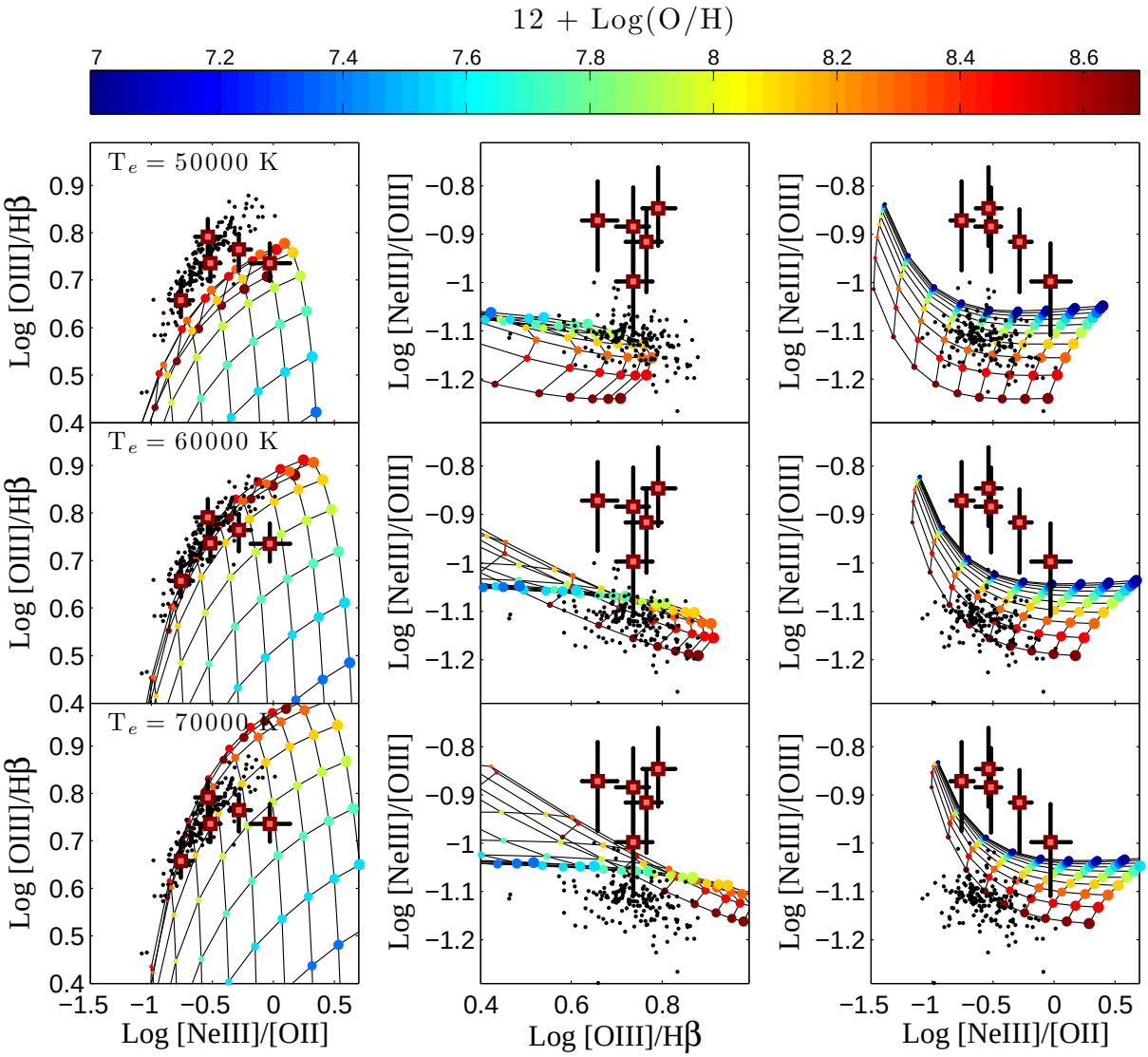

FIG. 7.— The line ratios of our high Hβ equivalent width local galaxies (black dots) and our stacks of $z \sim 2$ emission-line galaxies (red squares) compared to the predictions of CLOUDY models in three different projections of our emission-line space. The [Ne III]/[O III] measurements have been corrected for extinction using the Calzetti (2001) obscuration law. The points on the CLOUDY grid are color-coded by metallicity following the scale at the top of the diagram, with the size of each point proportional to the value of the ionization parameter. The density of the ISM has been held fixed at 10^3 cm^{-3}. From top to bottom the grids represent effective temperatures of 50,000, 60,000, and 70,000 K. Despite increasing the blackbody temperature to 70,000 K, the models are still unable to reproduce our stacked values.

$(7.1 < 12 + \log \mathrm{O/H} < 8.4)$.

On the other hand, ^{22}Ne has a different formation site: the hydrogen and helium burning shells of massive stars in their late stages of evolution. During a thermal pulse, some of the ^{12}C and ^{16}O produced by the fusion of helium can be convected outward to the site of the temporarily dormant hydrogen burning shell. When the hydrogen re-ignites, this material will be converted to ^{14}N via CNO burning, and, upon the next thermal pulse, some of this nitrogen will be transported back to into the helium burning shell, where it will undergo α captures. The result is the creation of ^{18}O, ^{22}Ne, ^{25}Mg, and s-process elements. Dredge-up can then bring this material to the stellar surface, where it can be lost to the interstellar medium via stellar winds. If the importance of this process is greater in the $z \sim 2$ universe, the result can be an enhancement in the total neon to oxygen ratio.

Interestingly, the analysis of Galactic cosmic rays suggests a ^{22}Ne/^{20}Ne ratio of ~ 0.4, i.e., a value that is ~ 5.3 times higher than what is found in the solar wind (e.g., Binns et al. 2005). Although the cause of this offset is still debated, the most widely accepted explanation for the excess ^{22}Ne ions lies in the physics of carbon-rich Wolf-Rayet stars (Casse & Paul 1982; Prantzos et al. 1987). The high-velocity winds of these systems cannot only deposit the ^{22}Ne from shell mixing into the local ISM, but the wind interactions with standing shocks from nearby Wolf-Rayet and precursor OB stars can accelerate material to the high speeds associated with cosmic rays. Wolf-Rayet star winds have also been invoked to explain the high nitrogen to oxygen ratios observed at $z \sim 2$ (e.g., Masters et al. 2014; Shapley et al. 2014), though in this case, it is the nitrogen-rich WN stars which are the source of the enhancement.

If, indeed, ^{22}Ne is solely responsible for the elevated [Ne III]/[O III] line ratios observed in our *HST* grism galaxies, then the ^{22}Ne/^{20}Ne isotopic ratio at $z \sim 2$ must ~ 0.6. This is roughly ten times larger than that ratio seen in the Solar wind, and ~ 1.5 times larger than that measured for cosmic rays. At face value, such an enhancement does not seem plausible. However, many aspects of massive star stellar evolution, such as the evolution of the IMF with redshift, the effects of stellar rotation, and the importance of binary stars at high-z, are not well known. Moreover, it is not clear whether the solar ratio of ^{22}Ne/^{20}Ne is representative of the $z \sim 0$ universe as a whole: it is quite possible that the isotopic ratio in spiral arms is larger than that observed in the solar system. Thus, this possibility cannot be ruled out.

5.1.6. *Compton-Thick AGN*

Non-thermal radiation can enhance [Ne III] relative to [O III] and reproduce the line ratios seen at $z \sim 2$. As the bottom left panel of Figure 3 demonstrates, the local sample of galaxies classified as AGN by the MEx diagnostic (Juneau et al. 2011, 2014) clearly have enhanced values of [Ne III] relative to the locus of star-forming galaxies.

All three of our program fields — GOODS-N, GOODS-S, and COSMOS – have medium deep and deep X-ray data (Elvis et al. 2009; Alexander et al. 2003; Xue et al. 2011), and, at the redshifts considered here ($1.90 < z < 2.35$), X-rays associated with normal star formation will be well below the limits of detection (Lehmer et al. 2010). Consequently, any emission-line galaxy whose position is co-incident with an X-ray source is likely powered by an AGN.

To search for these AGN, we cross-correlated our $z \sim 2$ object catalog with the list of X-ray sources found in the COSMOS, GOODS-N, and GOODS-S regions. Only four of our emission-line galaxies lie within 2.5″ of an X-ray source, and, in all four, the signal-to-noise ratio is too low to place a significant limit on [Ne III]/[O III]. We then stacked the remaining 63 galaxies in the Chandra Deep Field South 4Ms field (Xue et al. 2011) following the procedure described by Luo et al. (2011), and examined the resulting image for evidence of X-ray emission. No X-rays were found down to 90% upper limits of 3.2×10^{-18}, 6.7×10^{-18}, and 6.8×10^{-18} ergs s^{-1} cm^{-2} for the 0.5-2.0 keV, 2.0-8.0 keV, and 0.5-8.0 keV bandpasses, respectively. These limits correspond to a maximum absorbed X-ray luminosity of $\sim 2 \times 10^{41}$ ergs s^{-1} at the average redshift of the stacked sample ($z = 2.09$) and constrain the maximal fractional contribution of AGN to the observed [O III] and [Ne III] luminosities.

Xue et al. (2012) has argued that 20-25% of the cosmic hard X-ray background (6-8 keV) emanates from heavily obscured AGN residing in low mass (2×10^8 to $2 \times 10^9\, M_\odot$), high redshift ($1 < z < 3$) galaxies, with an average 0.5-2 keV flux of 1.43×10^{-18} erg cm^{-2} s^{-1}. This is below the 90% upper limit found in our stacking analysis, so it remains possible that the high [Ne III]/[O III] ratios are being caused by obscured AGN. This is illustrated in Figure 8, which uses the *Chandra* Proposal Planning Toolkit[8] to show our intrinsic X-ray luminosity limit as a function of absorbing column density, N_H, for an AGN with photon power law index of $\Gamma = 1.9$.

To better quantify the effect of AGN on the observed [Ne III]/[O III] ratio, we can begin by considering our median $z \sim 2$ galaxy, which has an extinction-corrected [O III] luminosity of $\sim 5 \times 10^{42}$ ergs s^{-1}. Compton-thin AGN with 2-8 keV luminosities near the limit of our stacking analysis ($L \sim 2 \times 10^{41}$ ergs s^{-1}) typically have [O III] to X-ray luminosity ratios of between ~ 0.01 and 0.1 (Lamastra et al. 2009; Wilkes et al. 2013). This means that these objects can contribute no more $\sim 0.4\%$ to the total [O III] luminosity of our stacked galaxy. In contrast, Compton-thick AGN can have [O III] to X-ray luminosity ratios that are ~ 100 times larger (Wilkes et al. 2013), hence their contribution could conceivably be as large as $\sim 40\%$. If we let $\eta_{\rm SF} = 0.078 \pm 0.001$ be the mean [Ne III]/[O III] ratio for our local sample of high-equivalent width star forming galaxies, and $\eta_{\rm AGN} = 0.21$ be the same quantity for local Seyfert 1 AGN (Nagao et al. 2001), then the measured [Ne III]/[O III] ratio in our $z \sim 2$ stacked galaxy should be

$$\eta_{\rm obs} = \frac{\eta_{\rm SF} + f\eta_{\rm AGN}}{1+f} \quad (1)$$

where f is the median fractional contribution of AGN to the luminosity of [O III]. For $f \lesssim 0.4$, $\eta_{\rm obs} \lesssim 0.116$, so this is still consistent with the measured values of our stacks. This argument holds for any distribution of the fractional contribution of AGN to the luminosity of [O III] as long as the median of that distribution is a few tens of percent. We therefore cannot rule out the hypothesis that an unseen population of Compton-thick AGN is causing the $z \sim 2$ [Ne III]/[O III] line ratios to appear enhanced.

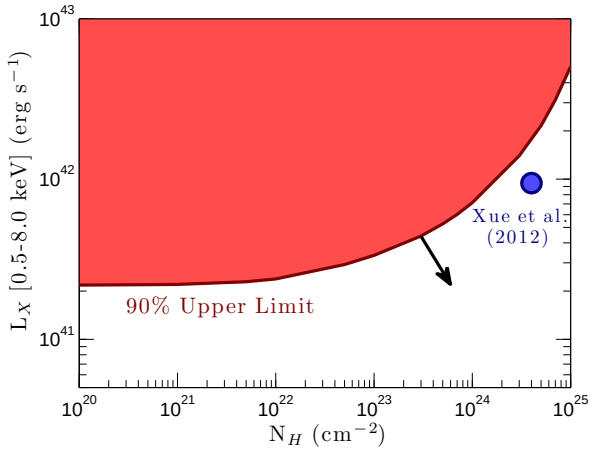

FIG. 8.— The intrinsic X-ray luminosity for 0.5-8.0 keV (L_X) is plotted against the absorbing hydrogen column density (N_H) for the 90% upper limit found in our X-ray stacking analysis. The upper limit curve is plotted in dark red and the region ruled out by the stacking analysis is shown in light red. The arrow indicates the phase-space still allowed. Xue et al. (2012) performed an X-ray stacking analysis and found that Compton-thick AGN ($N_H \sim 4\times10^{24}$ cm^{-2}) at $z = 1-3$ with $2\times10^8 < M_*/M_\odot < 2\times10^9$ likely produce 20%-25% of the 6-8 keV cosmic X-ray background. The stacked X-ray luminosity of these sources is shown as a blue dot.

[8] http://cxc.harvard.edu/toolkit/pimms.jsp

6. FUTURE AVENUES

When comparing the median stacked values for our 236 $z \sim 2$ galaxies to a local comparison sample from SDSS (well-matched in stellar mass and sSFR), we find consistent [O III]/Hβ ratios across all stellar masses. However, [Ne III]/[O II] is elevated by 0.23 ± 0.13 dex for $\log M_*/M_\odot \lesssim 9$ and [Ne III]/[O III] is persistently high by more than $1.5\,\sigma$ (0.16 to 0.25 dex) for each mass bin and all reasonable extinction laws with a total significance of $3.6\,\sigma$. There are several possible mechanisms that can explain the high ratios, including oxygen depletion, extreme densities, and the existence of a large population of X-ray obscured AGN. Further observations with current ground-based 8-m class telescopes as well as upcoming space-based missions like the *James Webb Space Telescope* are required to assess whether the elevation is truly compelling and to identify the physical reasons for it.

The ratio of [Ne III]/[O III] is sensitive to dust, and although we were able to estimate the attenuation through the indirect method of stellar reddening, measurements of the Balmer decrement would allow an accurate correction. Hβ, Hγ, and Hδ are all observable in our stacked spectra, but due to their low signal-to-noise ratio, short lever arm, and the effects of stellar absorption, these ratios yield highly uncertain extinction estimates. A measurement of Hα placed on the same relative flux scale as Hβ can be obtained from the ground via the MOSFIRE instrument on Keck (McLean et al. 2012) and the FLAMINGOS-2 spectrograph on Gemini (Eikenberry et al. 2012). This would remove the uncertainty associated with extinction.

We explored the possibility that the ratio of [Ne III]/[O III] could be caused by collisional de-excitation of [O III] at high electron densities ($\gtrsim 10^5$ cm^{-3}). This would only be possible in a multi-zonal model as a single zone ionized region cannot explain all three observed line ratios. If indeed H II regions in the $z \sim 2$ universe are clumpier than their local counterparts, high critical density UV emission lines such as CIII]λ1909 may show strong emission. A CIII] equivalent width of 10Å (Stark et al. 2014) would translate into a median expected flux of $\sim 3\times10^{-18}$ ergs s^{-1} cm^{-2}.

Further investigations of the [Ne III]/[O III] ratio are also possible for $1.3 \lesssim z \lesssim 1.6$ using GOODS-N archival data from the WFC3 G102 (PI Barro: GO-13420) and G141 grisms. The G102 grism also provides a measurement of the higher ionization line [Ne V] λ3426 for nearly 100 of the galaxies in our sample. Since AGN exhibit [Ne V]/[Ne III] ratios that are an order of magnitude greater than that of normal star-forming systems, these data could be used to test whether obscured AGN are responsible for enhanced [Ne III] emission in the $z \sim 2$ universe.

We would like to thank the anonymous referee for their fantastic input and comments on the manuscript. This work was supported via NSF through grant AST 09-26641 and AST 08-07873. The Institute for Gravitation and the Cosmos is supported by the Eberly College of Science and the Office of the Senior Vice President for Research at the Pennsylvania State University. This work is based on observations taken by the 3D-HST Treasury Program (GO 12177 and 12328) with the NASA/ESA HST, which is operated by the Association of Universities for Research in Astronomy, Inc., under NASA contract NAS5-26555.

REFERENCES

Abazajian, K.N., Adelman-McCarthy, J.K., Agüeros, M.A., et al. 2009, ApJS, 182, 543
Acquaviva, V., Gawiser, E., & Guaita, L. 2011, ApJ, 737, 47
Acquaviva, V., 2012, private communication
Alexander, D.M., Bauer, F.E., Brandt, W.N., et al. 2003, AJ, 126, 539
Asplund, M., Grevesse, N., Sauval, A.J., & Scott, P. 2009, ARA&A, 47, 481
Baldwin, J.A., Phillips, M.M., & Terlevich, R. 1981, PASP, 93, 5
Bertin, E., & Arnouts, S. 1996, A&AS, 117, 393
Binette, L., Dopita, M. A., & Tuohy, I. R. 1985, ApJ, 297, 476
Binns, W. R., Wiedenbeck, M. E., Arnould, M., et al. 2005, ApJ, 634, 351
Brammer, G.B., van Dokkum, P.G., Franx, M., et al. 2012, ApJS, 200, 13
Bruzual, G., & Charlot, S. 2003, MNRAS, 344, 1000
Calzetti, D. 2001, PASP, 113, 1449
Cardamone, C., Schawinski, K., Sarzi, M., et al. 2009, MNRAS, 399, 1191
Casse, M., & Paul, J. A. 1982, ApJ, 258, 860
Chabrier, G. 2003, PASP, 115, 763
Dessart, L., Crowther, P. A., Hillier, D. J., et al. 2000, MNRAS, 315, 407
Dopita, M.A., Fischera, J., Sutherland, R.S., et al. 2006, ApJ, 647, 244
Eikenberry, S., Bandyopadhyay, R., Bennett, J.G., et al. 2012, Proc. SPIE, 8446, 8446OI
Elvis, M., Civano, F., Vignali, C., et al. 2009, ApJS, 184, 158
Eracleous, M., Boroson, T. A., Halpern, J. P., & Liu, J. 2012, ApJS, 201, 23
Erb, D.K., Steidel, C.C., Shapley, A.E., et al. 2006, ApJ, 647, 128
Evans, I.N., & Dopita, M.A. 1985, ApJS, 58, 125
Ferland, G.J., Korista, K.T., Verner, D.A., et al. 1998, PASP, 110, 761
Ferland, G.J., Porter, R.L., van Hoof, P.A.M., et al. 2013, å, 49, 137
Förster Schreiber, N.M., Genzel, R., Bouché, N., et al. 2009, ApJ, 706, 1364
Francis, P.J., Hewett, P.C., Foltz, C.B., et al. 1991, ApJ, 373, 465
Fruchter, A., Sosey, M., Hack, W., et al. 2009, The MultiDrizzle Handbook Version 3.0 (Baltimore, STScI)
Garnett, D.R. 2002, arXiv:astro-ph/0211148
Gebhardt, H., Zeimann, G.R., Ciardullo, R., et al. 2014, in preparation
Giavalisco, M., Ferguson, H.C., Koekemoer, A.M., et al. 2004, ApJ, 600, L93
Grogin, N.A., Kocevski, D.D., Faber, S.M., et al. 2011, ApJS, 197, 35
Groves, B. A., Dopita, M. A., & Sutherland, R. S. 2004, ApJS, 153, 9
Groves, B., Brinchmann, J., & Walcher, C.J. 2012, MNRAS, 419, 1402
Hagen, A., Ciardullo, R., Gronwall, C., et al. 2014, ApJ, 786, 59
Hao, C.N., Kennicutt, R.C., Johnson, B.D., et al. 2011, ApJ, 741, 124
Henry, R.B.C. 1989, MNRAS, 241, 453
Holden, B.P., Oesch, P.A., Gonzalez, V.G., et al. 2014, submitted to ApJ (arXiv:1401.5490)
Hunt, L.K., & Hirashita, H. 2009, A&A, 507, 1327
Ioppolo, S., Cuppen, H. M., Romanzin, C., van Dishoeck, E. F., & Linnartz, H. 2008, ApJ, 686, 1474
Izotov, Y.I., Stasińska, G., Meynet, G., Guseva, N.G., & Thuan, T.X. 2006, A&A, 448, 955
Izotov, Y.I., Guseva, N.G., & Thuan, T.X. 2011, ApJ, 728, 161

Jenkins, E.B. 2009, ApJ, 700, 1299
Juneau, S., Dickinson, M., Alexander, D.M., & Salim, S. 2011, ApJ, 736, 104
Juneau, S., Bournaud, F., Charlot, S., et al. 2014, ApJ, 788, 88
Kennicutt, R.C., Jr. 1984, ApJ, 287, 116
Kennicutt, R.C., & Evans, N.J. 2012, ARA&A, 50, 531
Kewley, L.J., & Dopita, M.A. 2002, ApJS, 142, 35
Kroupa, P. 2001, MNRAS, 322, 231
Kümmel, M., Walsh, J.R., Pirzkal, N., Kuntschner, H., & Pasquali, A. 2009, PASP, 121, 59
Lamastra, A., Bianchi, S., Matt, G., et al. 2009, A&A, 504, 73
Lehmer, B.D., Alexander, D.M., Bauer, F.E., et al. 2010, ApJ, 724, 559
Leitherer, C., Schaerer, D., Goldader, J.D., et al. 1999, ApJS, 123, 3
Levesque, E.M., & Richardson, M.L.A. 2014, ApJ, 780, 100
Luo, B., Brandt, W.N., Xue, Y.Q., et al. 2011, ApJ, 740, 37
Madau, P. 1995, ApJ, 441, 18
Mannucci, F., Cresci, G., Maiolino, R., et al. 2009, MNRAS, 398, 1915
Massey, P., Puls, J., Pauldrach, A.W.A., et al. 2005, ApJ, 627, 477
Masters, D., McCarthy, P., Siana, B., et al. 2014, ApJ, 785, 153
McLean, I.S., Steidel, C.C., Epps, H.W., et al. 2012, Proc. SPIE, 8446
Mendez, A.J., Coil, A.L., Aird, J., et al. 2013, ApJ, 770, 40
Moustakas, J., Kennicutt, R.C., Jr., & Tremonti, C.A. 2006, ApJ, 642, 775
Murphy, E.J., Condon, J.J., Schinnerer, E., et al. 2011, ApJ, 737, 67
Nagao, T., Murayama, T., & Taniguchi, Y. 2001, PASJ, 53, 629
Nakajima, K., & Ouchi, M. 2014, MNRAS, 442, 900
Netzer, H., Mainieri, V., Rosati, P., & Trakhtenbrot, B. 2006, A&A, 453, 525
Nonino, M., Dickinson, M., Rosati, P., et al. 2009, ApJS, 183, 244
Osterbrock, D.E., & Ferland, G.J. 2006, Astrophysics of Gaseous Nebulae and Active Galactic Nuclei, 2nd. ed. by D.E. Osterbrock & G.J. Ferland (Sausalito, CA: University Science Books)
Prantzos, N., Arnould, M., & Arcoragi, J.-P. 1987, ApJ, 315, 209
Price, S. H., Kriek, M., Brammer, G. B., et al. 2014, ApJ, 788, 86
Rodighiero, G., Daddi, E., Baronchelli, I., et al. 2011, ApJ, 739, L40
Salpeter, E.E. 1955, ApJ, 121, 161
Scoville, N., Aussel, H., Brusa, M., et al. 2007, ApJS, 172, 1
Shapley, A. E., Reddy, N. A., Kriek, M., et al. 2014, submitted to ApJ (arXiv:1409.7071)
Shirazi, M., Brinchmann, J., & Rahmati, A. 2014, ApJ, 787, 120
Skelton, R. E., Whitaker, K. E., Momcheva, I. G., et al. 2014, ApJS, 214, 24
Smith, J.-D. T., & Houck, J. R. 2005, ApJ, 622, 1044
Snijders, L., Kewley, L.J., & van der Werf, P.P. 2007, ApJ, 669, 269
Solomon, P.M., Downes, D., & Radford, S.J.E. 1992, ApJ, 387, L55
Stark, D. P., Richard, J., Siana, B., et al. 2014, arXiv:1408.1420
Steidel, C.C., Rudie, G.C., Strom, A.L., et al. 2014, ApJ in press (arXiv:1405.5473)
Sutherland, R. S., & Dopita, M. A. 1993, ApJS, 88, 253
Taniguchi, Y., Scoville, N., Murayama, T., et al. 2007, ApJS, 172, 9
Teplitz, H.I., Malkan, M.A., Steidel, C.C., et al. 2000, ApJ, 542, 18
Tielens, A.G.G.M. 2008, ARA&A, 46, 289
Timmes, F.X., Woosley, S.E., & Weaver, T.A. 1995, ApJS, 98, 617
Vargas, C.J., Bish, H., Acquaviva, V., et al. 2014, ApJ, 783, 26
Vázquez, G.A., & Leitherer, C. 2005, ApJ, 621, 695
Weiner, B. J., & AGHAST Team 2014, American Astronomical Society Meeting Abstracts #223, 223, #227.07
Whitaker, K.E., Franx, M., Leja, J., et al. 2014, submitted to ApJ (arXiv:1407.1843)
Wilkes, B. J., Kuraszkiewicz, J., Haas, M., et al. 2013, ApJ, 773, 15
Willis, A. J., Dessart, L., Crowther, P. A., et al. 1997, MNRAS, 290, 371
Willis, A. J. 1999, Wolf-Rayet Phenomena in Massive Stars and Starburst Galaxies, 193, 1
Woosley, S.E., & Weaver, T.A. 1995, ApJS, 101, 181
Wuyts, S., Förster Schreiber, N.M., Nelson, E.J., et al. 2013, ApJ, 779, 135
Xue, Y.Q., Luo, B., Brandt, W.N., et al. 2011, ApJS, 195, 10
Xue, Y. Q., Wang, S.X., Brandt, W.N., et al. 2012, ApJ, 758, 129
York, D. G., Adelman, J., Anderson, J. E., Jr., et al. 2000, AJ, 120, 1579
Zeimann, G.R., Ciardullo, R., Gebhardt, H., et al. 2014, ApJ, 790, 113

TABLE 1
Physical Characteristics of Median Stacked Spectra

⟨Log M_*⟩ $M_\odot$	Num. —	⟨SFR⟩ $M_\odot$ yr^{-1}	⟨Log sSFR⟩ yr^{-1}	⟨β⟩ —	Log [O III]/Hβ —	Log [Ne III]/[O II] —	Log [Ne III]/[O III] Obs.	Log [Ne III]/[O III] Cor.[a]
7.87	47	2.0	−7.47	−2.04	0.74±0.05	−0.03±0.16	−1.02±0.09	−1.00±0.10
8.45	47	3.7	−7.93	−1.98	0.76±0.04	−0.28±0.09	−0.97±0.10	−0.92±0.09
8.89	48	8.2	−8.01	−1.74	0.79±0.04	−0.54±0.11	−0.98±0.10	−0.85±0.08
9.20	47	11.8	−8.08	−1.80	0.74±0.04	−0.52±0.11	−0.96±0.10	−0.89±0.09
9.58	48	32.6	−8.07	−1.53	0.66±0.05	−0.76±0.10	−1.04±0.09	−0.87±0.09

[1] [Ne III]/[O III] corrected for extinction via a Calzetti (2001) obscuration law using the UV slope.

TABLE 2
Line Ratio Comparison between $z \sim 2$ and $z \sim 0$

Mass Bin Log ($M_*/M_\odot$)	Num. $z \sim 2$	Num. $z \sim 0$	Log [O III]/Hβ Offset[a]	Log [Ne III]/[O II] Offset[a]	Log [Ne III]/[O III][b] Offset[a]
7.50 - 8.18	47	11	+0.00±0.05	+0.33±0.20	+0.16±0.10
8.18 - 8.72	47	43	−0.00±0.04	+0.23±0.10	+0.22±0.09
8.72 - 9.07	48	40	+0.06±0.04	+0.09±0.11	+0.26±0.08
9.07 - 9.35	47	59	−0.01±0.04	+0.05±0.11	+0.23±0.09
9.35 - 10.50	48	25	−0.05±0.05	−0.07±0.11	+0.23±0.09

[1] The difference between the logarithm of the median line ratios for the $z \sim 2$ sample and the local comparison sample with high equivalent widths.
[2] [Ne III]/[O III] corrected for extinction via a Calzetti (2001) obscuration law.